RSC Advances

PAPER

View Article Online
View Journal | View Issue

Cite this: RSC Adv., 2016, 6, 68371

In situ crosslinked PVA–PEI polymer binder for long-cycle silicon anodes in Li-ion batteries

Zhen Liu,†[a] Shaojie Han,†[b] Chong Xu,[a] Yuwen Luo,[a] Na Peng,[a] Chenyang Qin,[a] Mingjiong Zhou,*[a] Wenqin Wang,[a] Liwei Chen[b] and Shigeto Okada[c]

Received 11th May 2016
Accepted 13th July 2016

DOI: 10.1039/c6ra12232a

www.rsc.org/advances

A novel polymer binder, synthesized *via in situ* thermal cross-linking of water-soluble polyvinyl alcohol (PVA) and poly(ethylene imine) (PEI) precursor, is applied as a functional network binder to enhance the electrochemical performance of a silicon anode. The Si anode with PVA–PEI binder exhibits high specific capacity (3072.9 mA h g^{-1}) in the initial cycle, high initial coulombic efficiency of 83.8% and excellent long-term cycling stability (1063.1 mA h g^{-1} after 300 cycles). Furthermore, the Si anode containing PVA–PEI binder also exhibits excellent rate performance, reaching a high specific capacity of 1590 mA h g^{-1} even at high current density of 10 A g^{-1}. These outstanding electrochemical properties are ascribed to the reversibly-deformable polymer network and the binder's strong adhesion to the silicon particles. This low-cost and eco-friendly polymer binder has great potential to be used for silicon anodes in next generation Li-ion batteries.

1. Introduction

Lithium-ion batteries (LIBs) are the most promising energy storage devices for various technological applications, including portable electronic devices, hybrid electric vehicles (HEVs), electric vehicles (EVs), and smart energy utility grids.[1–5] However, the commercial graphite anode cannot enable the creation of batteries that achieve the high energy density required for EVs and HEVs, which has motivated research into new high-capacity anode materials.[6–8] Materials that can electrochemically form intermetallic alloys with Li are promising candidates due to their much higher theoretical capacities.[9–11] Among those, silicon (Si) has been extensively investigated due to its high theoretical capacity (~4200 mA h g^{-1}), low cost and low charge–discharge potential.[12–17] Unfortunately, silicon suffers from gigantic volume changes (~400%) during the lithiation/delithiation process, which causes pulverization and leads to isolation of the active material and instability of the solid-electrolyte interphase (SEI).[18–25] These in turn result in drastic capacity fading and low coulombic efficiency.[26–28] The situation becomes even worse when fabricating high-energy cells. Many efforts have been made to overcome these problems and improve the performance of Si anode. One of the main approaches is adopting nanostructured Si materials to better accommodate the strain during charge/discharge and thus alleviate the pulverization of active Si materials.[29–31] However, the SEI film generally still fails due to the intrinsic volume change of Si materials during cycling, leading to limited cycle life.

The binder, which is one of the most important components of an electrode, is used to bind active material and conductive carbon together onto the current collector. Recent studies have demonstrated that the polymer binder has a direct effect on the electrochemical performance of the electrodes, especially for the irreversible capacity and cyclability.[32–34] In commercial LIBs, the most frequently used binder is poly(vinylidene fluoride) (PVDF), which has strong adhesion with graphite and a wide electrochemical window. However, PVDF cannot robustly adhere to high-capacity electrodes that exhibit huge volume changes due to its non-functionalized linear chain structure.[32,34,35] A binder with better adhesion is thus needed to enable good cycle life for Si anodes. Recently, some functional binders such as polyacrylic acid (PAA) and carboxymethyl cellulose (CMC) were found to better adhere on silicon particles and better accommodate the volume changes. Multi-functional polymer binders were also developed to enhance the electrochemical properties of Si anodes. For example, Liu *et al.*[36] synthesized a conductive polymer binder for Si anodes to improve adhesion, ductility, and electrolyte-uptake. Nevertheless, the linear chain character of these polymer binders is susceptible to sliding upon the continual volume change of silicon during cycling and thus their performance has not met the requirements for practical application (*e.g.* long cycle life, high mass loading, and high coulombic efficiency). To

[a]School of Materials Science and Chemical Engineering, Ningbo University, Fenghua Road 818, Jiangbei District, Ningbo 315211, Zhejiang, China. E-mail: zhoumingjiong@nbu.edu.cn; Fax: +86-574-86600147; Tel: +86-574-86600147

[b]Suzhou Institute of Nano-Tech and Nano-Bionics, Chinese Academy of Sciences, Ruoshui Road 398, SEID, Suzhou Industrial Park, Suzhou 215123, Jiangsu, China

[c]Institute for Materials Chemistry and Engineering, Kyushu University, 6-1 Kasuga-koen, Kasuga 816-8580, Japan

† These authors contributed equally to this work.

overcome these issues, three-dimensional network polymers have been developed for silicon anodes, in which the polymer chain was anchored by a cross-linking technique. For example, Koo *et al.*[37] presented a thermally cured polymeric binder by chemical cross-linking of carboxymethylcellulose sodium (NaCMC) and PAA for a high-capacity Si anode. Ryou *et al.*[38] prepared mussel-inspired adhesive binders through conjugation of dopamine hydrochloride to sodium alginate (SA) and PAA to obtain high-capacity Si anodes. Song *et al.*[32] synthesized an interpenetrated gel polymer binder with a reversibly-deformable polymer network through *in situ* cross-linking of PAA and poly(vinyl alcohol) (PVA). These designs effectively improved the electrochemical properties of Si anodes by suppressing the adverse effects of their large volume expansion. Although several binders have been developed for Si anodes, the Si anodes with these binders still can not meet the demand of practical application in LIBs. Hence, development of novel binders is critical for realizing practical application of the Si anodes in LIBs.

Herein, we develop a novel, reversibly-deformable polymer binder for Si anode materials *via* an *in situ* thermal cross-linking approach. Considering cost and practical applications, water soluble PVA and poly(ethylene imine) (PEI) were selected binder precursors for this method. This polymer binder contains hydroxyl and imido functional groups, and thus can form an interconnected network that strongly bonds with Si particles (Fig. 1). Meanwhile, a relatively stable SEI is formed on the Si electrode with this binder during the cycling process as confirmed with atomic force microscopy (AFM). Excellent cycling stability and high rate performance were achieved by Si anodes with PVA–PEI binder. Therefore, the PVA–PEI binder provides a new binder-design perspective for Si-based anodes in LIBs.

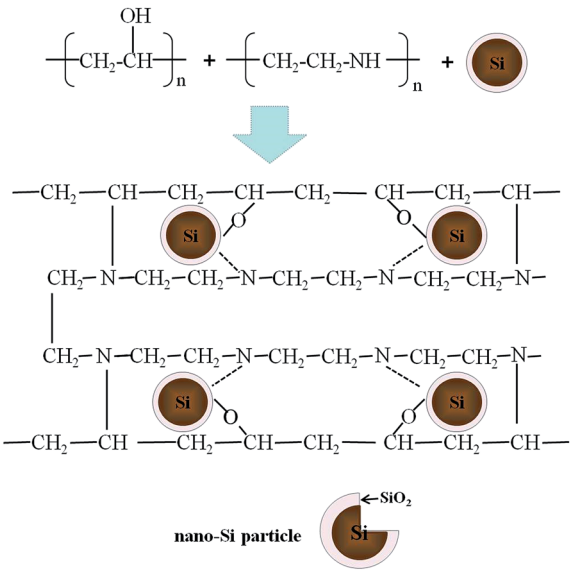

Fig. 1 The chemical structure and illustrative interaction between cross-linked PVA–PEI and silicon particles.

2. Experimental

Commercially available Si nanoparticles (~50 nm, Alfa Aesar) were applied as the active material without any further treatment. The poly(vinyl alcohol) (PVA) (Sigma Aldrich) and poly(ethylene imine) (PEI) (Aladdin) were purchased as the polymer binder precursors. The carboxymethyl cellulose (CMC) (Aladdin) and poly(vinylidene fluoride) (PVDF) (Sigma Aldrich) were utilized as control binders.

The aqueous solution of mixed poly(vinyl alcohol) and poly(ethylene imine) with the weight ratio of 8 : 2 was prepared as polymer binder precursor. For comparison, polyvinylidene fluoride (PVDF) solution of *N*-methyl-2-pyrrolidone (NMP) and aqueous solution of carboxymethyl cellulose (CMC) were utilized as control binders. To prepare the working electrode of a coin cell, the active material, conducting additive, and binder with the weight ratio of 6 : 2 : 2 were stirred for 4 h to form homogeneous slurry, and then the slurry was coated onto copper foil. Afterwards, the silicon electrode was dried at 100 °C for 8 h and then further thermally heated at 120 °C for 1 h in a vacuum oven. The amount of material on the Cu foil was in the range of 3–4.5 mg cm^{-2}, thus the active material loading is calculated to be *ca.* 1.8–2.7 mg cm^{-2}. The graphite anodes were prepared containing the active materials, Super P, and PVA–PEI binder in a ratio of 7 : 2 : 1 (weight ratio). Electrochemical properties were studied by using 2032 coin-type half cells assembled in Ar-filled glove box. Lithium foils and polypropylene films were used as counter electrodes and separators, respectively. The electrolyte (3015G, Guo Tai Hua Long Company) was 1 M $LiPF_6$ in a mixture of ethylene carbonate (EC) and dimethyl carbonate (DMC) (1 : 1 by volume). Galvanostatic charge and discharge tests were carried out at different constant current densities between 0.01 and 1.5 V using a LAND battery test system (Wuhan, China). After cycling, the coin cells were dissemabled and the test electrodes were washed and dried for characterization.

The phase of the as-purchased Si samples was characterized by using a Bruker D8 Advance diffractometer (XRD) with Cu Kα radiation, at 2θ range of 20–60° with 0.02 per step. The morphology and size of Si particles were determined by a NanoSEM 630 scanning electron microscope (SEM, Hitachi, Japan). Fourier transform infrared spectroscopy (FTIR) was carried out as diffuse reflectance measurements with powder samples using a Bruker IFS 66/S FT-IR spectrometer and Spectra-Tech Collector II DRIFTS accessory. An Agilent 5500 atomic force microscope (AFM) (Agilent Technologies, Santa Clara, CA) was applied to investigate the electrodes using silicon AFM tips (NSC18, Mikromasch, Tallinn, Estonia) with a resonance frequency of about 75 kHz and spring constant of about 2.8 N m^{-1}. For AFM characterization, the test electrodes were prepared and measured in an Ar-filled glove box. In addition, the surface morphology of electrodes were characterized by using SEM. The morphology of cycled Si electrode with PVA–PEI binder was investigated by transmission electron microscopy (TEM, Tecnai F20, FEI, America). Cross section of the samples soaked in liquid nitrogen were prepared by a microtome (Leitz

microtome type 1310, Germany) and fixed to a steel sample holder with adhesive tape without touching the surface.

3. Results and discussion

Fig. 2 shows SEM image and XRD pattern of raw silicon nanoparticles, combined with FTIR spectra of raw silicon nanoparticles. Commercial silicon nanoparticles having spherical shapes with an average size of ~50 nm were used in this study. The XRD pattern in Fig. 2 reveals the crystal structure of the Si nanoparticles. It is well known that Si nanoparticles are covered with a thin layer of amorphous SiO_2 because of oxidation when exposed to air.[34] To confirm this, FTIR analysis was carried out, as shown in Fig. 2. The peak at 3444 cm^{-1} was attributed to the hydrogen bonding of Si–OH groups. The peaks at 1179 cm^{-1} and 890 cm^{-1} corresponded to the Si–O–Si asymmetric stretching band and Si–O symmetric stretching band, respectively. These characteristic peaks agree well with the previous reports on the existence of an SiO_2 layer on the surface of Si nanoparticles.[32]

The silicon electrodes with the reversibly-deformable polymer binder were prepared by an *in situ* thermal polymerization approach. An aqueous solution of PVA and PEI (8 : 2, weight ratio) was used as precursors for the polymer binder. The electrodes were prepared by spreading a slurry of 60 wt% Si nanoparticles, 20 wt% carbon black, and 20 wt% polymer binder precursors in distilled water onto a Cu-foil current collector, and then dried in a vacuum oven. In this manner, the condensation reaction would take place between the hydroxyl groups of PVA and the imido groups of PEI. Simultaneously, the hydroxyl functional group of PVA would also react with the hydroxyl groups of SiO_2 on the surface of the Si particle. To verify the chemical structure of the network polymer binder, FTIR was carried out, as shown in Fig. 3. In the spectrum of PEI, the peaks at 3430 cm^{-1} and 1635 cm^{-1} originated from N–H bending.[39] For the PVA polymer, the peaks at 3439 cm^{-1} and 1704 cm^{-1} corresponded to the vibration of O–H groups, and the peak located in 1095 cm^{-1} was attributed to the C–O bond.[40] After cross-linking of PVA with PEI, it is clearly seen that the vibration peaks of O–H from the PVA (1704 cm^{-1} and 3439 cm^{-1}) and the peaks of N–H from the PEI (1635 cm^{-1} and 3430 cm^{-1}) were decreased. These changes demonstrated the formation of –CN– groups due to the condensation reaction of PVA and PEI, resulting in a cross-linked polymer network. In addition, the FTIR spectra of polymer films prepared with silicon showed obvious changes: the O–H bond peak of PVA at 1704 cm^{-1} completely disappeared and the stretching vibration peaks of the N–H bond of PEI at 1635 cm^{-1} were further reduced. Moreover, the stretching vibration peak of the C–O bond of PVA became broader, due to the appearance of stretching vibration peak of C–O–Si, which overlapped with the stretching vibration peak of C–O bond of PVA. These changes indicated the occurrence of the etherification reaction between the silicon particles and PVA, which confirmed the presence of interactions between the PVA–PEI binder and the Si particles. As identified in previous reports,[32] the strong interaction between binder and active Si material is beneficial for improving the electrode integrity and thus mitigating destruction of the electrical network under a large volume change during cycling.

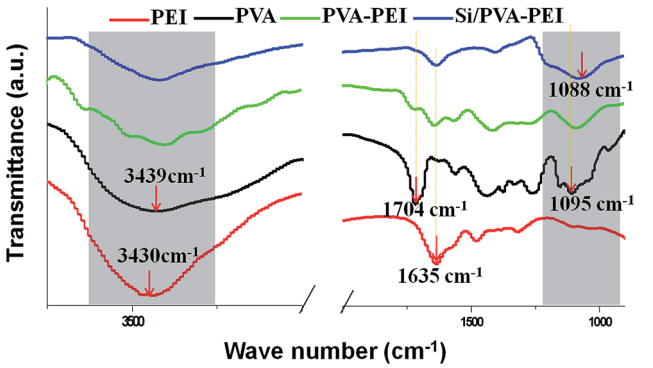

Fig. 3 The FTIR spectra of PVA, PEI, PVA–PEI mixed binder, and silicon/PVA–PEI composite.

CR2032 coin cells were used in charge–discharge measurements to study the electrochemical properties of the Si electrodes. To evaluate the PVA–PEI binder, PVDF and CMC binders were utilized in fabricating control electrodes prepared and tested following the same approach as the PVA–PEI binder. As shown in Fig. 4, the electrochemical properties of Si anodes with different binders were investigated. Fig. 4a shows the

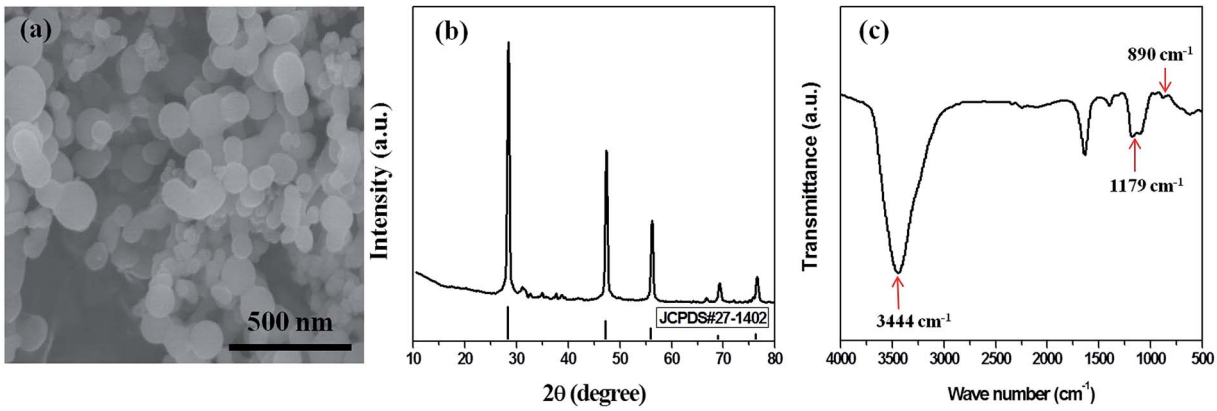

Fig. 2 (a) SEM image of raw silicon nanoparticles, (b) XRD pattern of raw silicon nanoparticles, and (c) FTIR spectra of raw silicon nanoparticles.

voltage profiles of the Si electrode with PVA–PEI binder for the 1st, 2nd, 5th, 50th, 100th, 200th and 300th galvanostatic discharge–charge cycles. In the first cycle, discharge potential showed a plateau at 0.1–0.01 V, consistent with the behavior of crystalline Si. The first discharge and charge capacities were 3072.9 mA h g^{-1} and 2575.1 mA h g^{-1}, respectively, with an initial coulombic efficiency of 83.8%. This excellent performance of Si anode demonstrated that this polymer binder is suitable for practical applications with its great bonding capability. Subsequently, the capacity at the 2nd, 5th, 50th, 100th, 200th, and 300th cycle, compared to the 1st charge capacity, was 98.4%, 96.5%, 82.6%, 72.2%, 54.5% and 41.3%, respectively. The comparison of cycling stability and coulombic efficiency of the electrodes with different binders further reflected the advantage of PVA–PEI binder. The cycling stability and coulombic efficiency of both the PVA–PEI electrode and control electrodes, cycled at a current density of 1 A g^{-1}, are shown in Fig. 4b. The capacity of the cell with PVDF binder significantly decreased with the cycling (40.6 mA h g^{-1} after 50 cycles). The Si anode with CMC binder showed an initial capacity of 2910.8 mA h g^{-1} and a better cycling stability (343.6 mA h g^{-1} after 300 cycles) than that with PVDF binder, but was still obviously unsatisfactory. In contrast, the Si anode with the PVA–PEI binder exhibited an excellent performance. A high initial capacity of 3072.9 mA h g^{-1} was achieved, which is about 73.2%

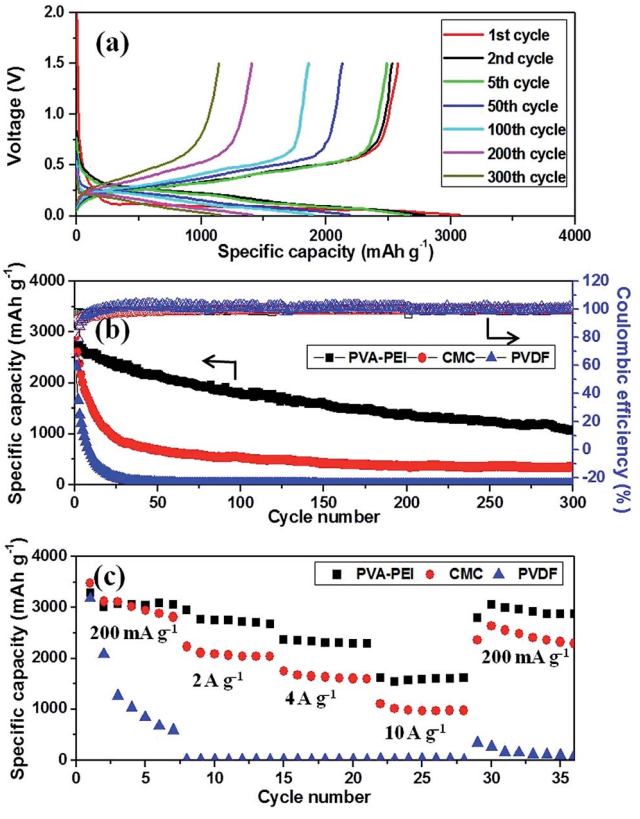

Fig. 4 (a) The charge/discharge voltage profiles of the silicon anode using PVA–PEI polymer binder; (b) the cycling performance and the coulombic efficiency of Si anodes with PVA–PEI, CMC, and PVDF binders, and (c) the rate performance (current density form 200 mA g^{-1} to 10 A g^{-1}) of electrodes with PVA–PEI, CMC, and PVDF binder.

of the theoretical capacity (~4200 mA h g^{-1}). After 300 cycles, the specific capacity remained over 1060 mA h g^{-1}, which is about 3 times the theoretical capacity of graphite. Furthermore, the Si electrode with the PVA–PEI binder also showed a relatively high initial coulombic efficiency of 83.8%, which increased to ~97.7% at the 2nd cycle, and further increased to ~98.9% at the 10th cycle, and finally stabilized at ~99.3% in subsequent cycles. The high coulombic efficiency and stable cycling of the silicon anode with the PVA–PEI polymer binder suggests that there exists a relatively stable SEI layer, which prevents the reaction between the electrolyte and the lithium.

In addition to the comparison of cycle ability, the rate capabilities of the electrodes with PVDF, CMC and PVA–PEI binder were also investigated at increasing current densities from 200 mA g^{-1} to 10 A g^{-1}. As shown in Fig. 4c, the Si anode with PVDF binder had hardly any capacity at high current densities and recovers poorly when a lower rate is again used. The rate capability of Si anode with CMC binder was better than that with PVDF binder, retaining a specific capacity of ~990 mA h g^{-1} at a high current density of 10 A g^{-1}. The Si anode with PVA–PEI binder had the best rate performance among the three. The cell exhibited a capacity of ~1590 mA h g^{-1} at high current density of 10 A g^{-1}, and recovered to the previous capacity of ~2798.5 mA h g^{-1} when the rate returned to 200 mA g^{-1}. Similar to the high coulombic efficiency and excellent cycling stability, the sufficient high rate capability of the silicon anode with PVA–PEI binder should be closely related to a stable SEI film formed on the Si anode even cycled at the high current density.

To verify the above hypothesis, AFM was employed to visualize the SEI morphology on Si anodes. The samples with different binders before cycling and after 100 cycles were transferred to an Agilent 5500 AFM to quantitatively investigate the topography of SEI film on the Si electrodes. AFM tips with a resonant frequency of about 75 kHz and spring constant of about 2.8 N m^{-1} were used as the probes. Fig. 5a–f shows AFM mappings of the silicon electrodes before and after cycling, together with the corresponding surface roughness of the Si electrodes (Fig. 5g). The original Si electrodes with PVDF, CMC, and PVA–PEI binder (Fig. 5a–c), exhibited granular morphology with ~81.7, 56.1 and 57.3 nm surface roughness, respectively. The Si electrodes with CMC and PVDF binders showed similar granular distribution, while the electrode with PVA–PEI binder was more compact than those using CMC and PVDF binders. Fig. 5d–f show corresponding electrode statuses after 100 cycles. As shown in Fig. 5d, the AFM mapping of electrode containing PVDF binder was very indistinct, and its roughness dropped to 35.6 nm. It is necessary to point out that a seriously trailing phenomenon happened during the scanning, which made the imaging process very difficult. Since the nanostructured Si materials can accommodate the strain and alleviate their pulverization during charge/discharge, it is plausible that those small and compact grains at surface are a thick SEI layer formed on the Si particles. Compared to the electrode with PVDF binder, the AFM mapping of the electrode with CMC binder was better (Fig. 5e). However, the surface roughness of electrode also decreased to 32.1 nm and SEI gathering regions

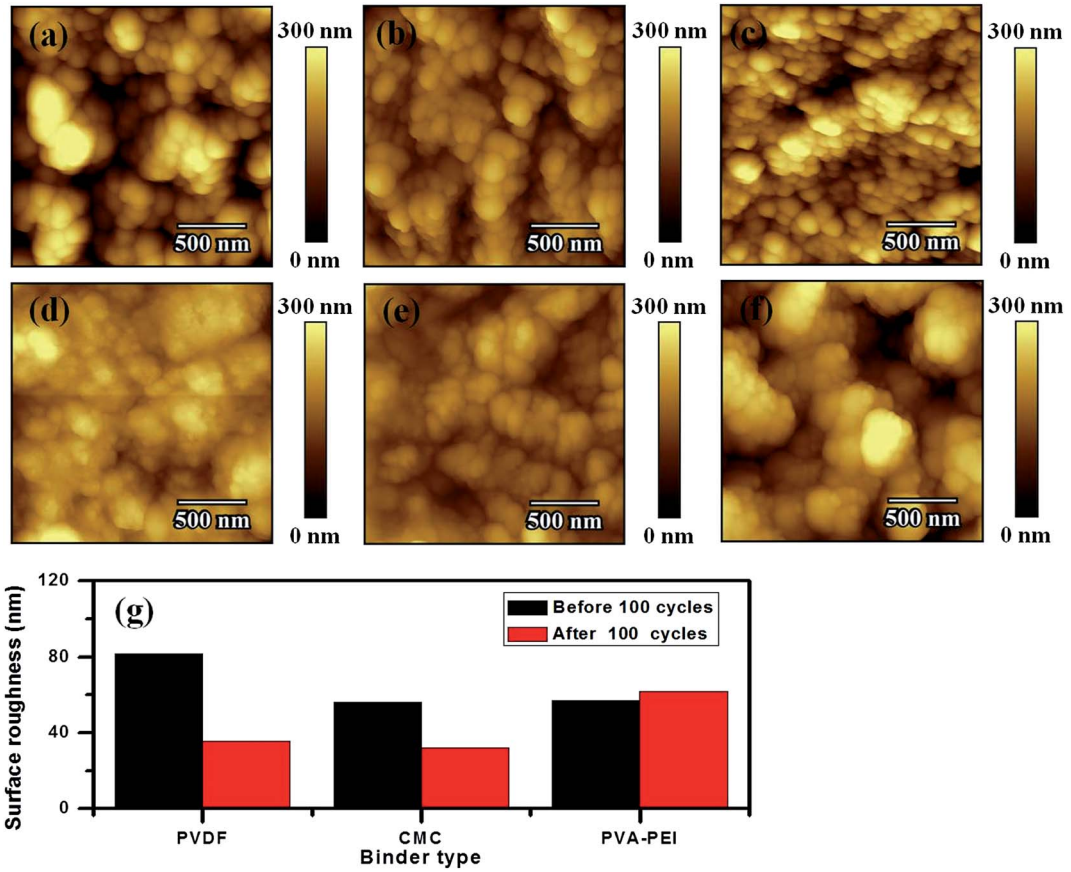

Fig. 5 The AFM images ($2 \times 2\ \mu m^2$ scan size) of the Si electrode surface (a–c) before cycling and (d–f) after 100 cycles with (a and d) PVDF, (b and e) CMC, and (c and f) PVA–PEI binders, and (g) the calculated surface roughness for all these conditions.

were observed. In contrast, the surface roughness of the electrode with PVA–PEI binder increased to 61.8 nm, which can be attributed to the mutual adhesion of Si particles and the formation of secondary particles with larger size after cycling (Fig. 5f). We believe that the Si particles were constrained by the PVA–PEI polymer network, by which these nanoparticles closely integrated together with carbon blacks during the cycling process. This could have increased interparticle contact and was beneficial to electron transfer, resulting in improved electrochemical performance. Furthermore, due to the tight encapsulation of the PVA–PEI polymer network, the contact area between the Si particles and electrolyte are greatly reduced. It can effectively suppress the formation of SEI film, as shown in Fig. 5f. Therefore, the cross-linked network of the PVA–PEI binder can help alleviate the issues caused by volume change of Si.

The Si anode materials are well known to suffer from substantial volume change during lithiation/delithiation, which cause severe pulverization of the silicon and continuous formation of a SEI.[41–44] It is widely accepted that a stable SEI ploys an active role in the electrochemical properties for Si anodes.[45–48] Based on these considerations, SEM studies were carried out on the Si electrodes with different binders before and after cycling, as shown in Fig. 6. For the pristine samples, all the electrodes had similar morphology: silicon nanoparticles and carbon black were uniformly dispersed on the copper foil (Fig. 6a–c). As expected, morphology changes were observed for all electrodes after 300 cycles. A large smooth surface topography was observed for the electrodes with PVDF and CMC binders, as marked by arrows in Fig. 6d and e. The smooth surface is believed to be due to the constant growth of a new SEI layer after particle pulverization and SEI failure. For the electrode with the PVA–PEI binder, neither obviously detectable morphology change nor microstructural failure was found, even after 300 cycles (Fig. 6f). These SEM images were highly consistent with the analysis of the AFM results (Fig. 5) that the SEI film formed on the Si particles with the PVA–PEI binder is more stable than those formed when using PVDF and CMC binders. The formation of the stable SEI could be attributed to the deformable feature of the PVA–PEI binder, which can effectively accommodate the large volume variation of Si particles during cycling, and prevent the further formation of new SEI film due to reaction between newly exposed silicon surface and electrolyte. Furthermore, the binder's strong adhesion to the silicon nanoparticles should assist in constructing a stable SEI for Si electrodes.

To validate the ability of the binder for accommodating large volume changes during cycling, the thickness variations of the silicon electrode with different binders were observed by SEM. Fig. 7a–c displays the cross-section SEM images of silicon

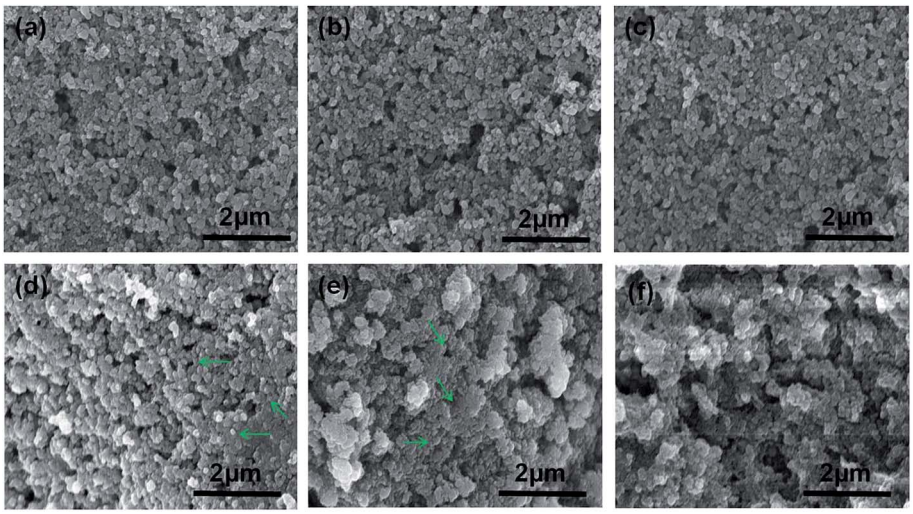

Fig. 6 SEM images of the surface morphology of the silicon electrodes with (a and d) PVDF, (b and e) CMC, and (c and f) PVA–PEI binder (a–c) before cycling and (d–f) after 300 cycles.

electrodes with different binders before cycling, at the end of the 5th discharge, and at the end of the 5th charge, respectively. As shown in Fig. 7a, the initial thickness of the electrode with PVA–PEI was about 44.8 μm, and the thickness increased to *ca.* 63.3 μm at the end of the 5th discharge, which was ~41% volume change. As the lithium extracted from the electrode, the expanded silicon nanoparticles shrank and the final thickness of the electrode was 48.2 μm, which almost returned to its

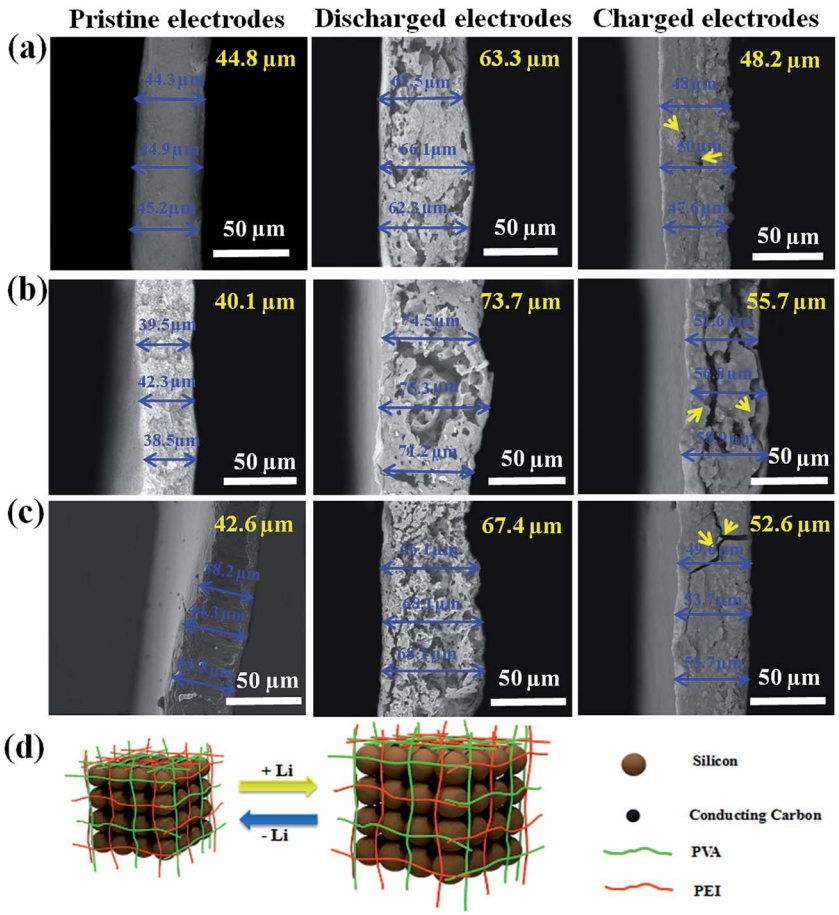

Fig. 7 Cross-sectional SEM images of the silicon electrodes with (a) PVA–PEI binder, (b) PVDF binder and (c) CMC binder before cycling, at the end of the 5th discharge, and at the end of the 5th charge, and (d) the proposed working mechanism of PVA–PEI binder for silicon electrodes.

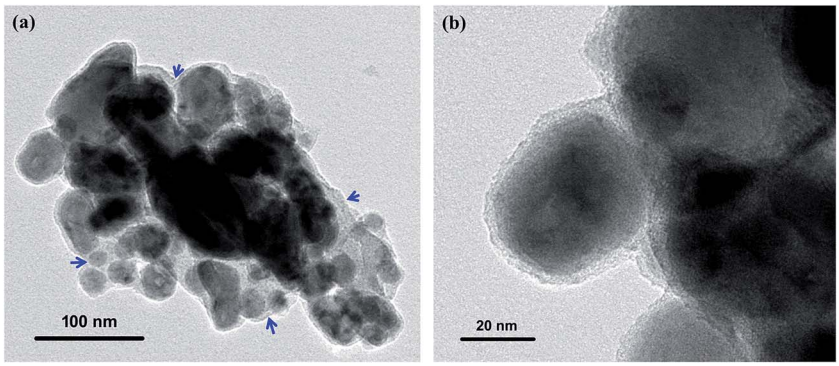

Fig. 8 (a) TEM image of the silicon electrode powder with PVA–PEI polymer binder after 5 cycles; (b) magnified TEM image of the silicon electrode powder with PVA–PEI polymer binder after 5 cycles.

original thickness with a volume change of ~7.6%. In contrast, as shown in Fig. 7b and c, the thickness of the silicon electrodes in the charged state after cycling with PVDF and CMC binder increased by ~38.9% and ~23.4%, respectively, which are ~3 times higher than the increase with PVA–PEI binder. Furthermore, many cracks were seen in the cross-sectional views and delamination of the electrodes from the current collector was also observed, which likely caused the high resistance and polarization of these electrodes. As schematically illustrated in Fig. 7d, the PVA–PEI polymer binder displays the most reversible deformation upon volume change of Si of all three binders thanks to its three-dimensional interpenetrated network. Furthermore, the effect of the cycling process on the binding between the Si particles and binder was examined by TEM. Fig. 8 shows the TEM images of the Si electrode with PVA–PEI binder after 5 cycles. It was clear that the Si particles are uniformly covered by binder (the edge is marked by arrows), which indicated that the connection between the Si particles and the binder was good even after the lithiation/delithiation processes. The results strongly confirmed the above suggestion of Fig. 7.

To further evaluate the effect of PVA–PEI binder, the electrochemical property of a graphite anode was also studied. Fig. 9 shows the cycling stability of graphite electrode with PVA–PEI binder at a current of 100 mA g^{-1}. The initial discharge and charge capacities were 365.7 and 329.5 mA h g^{-1}, respectively, which correspond to an initial coulombic efficiency of 90.1%. Moreover, the graphite anode also showed an excellent capacity retention upon to 30 cycles. These results further demonstrated that the water soluble, cross-linked polymer binder has a good compatibility with commercial Li-ion batteries, which makes it more promising for practical application.

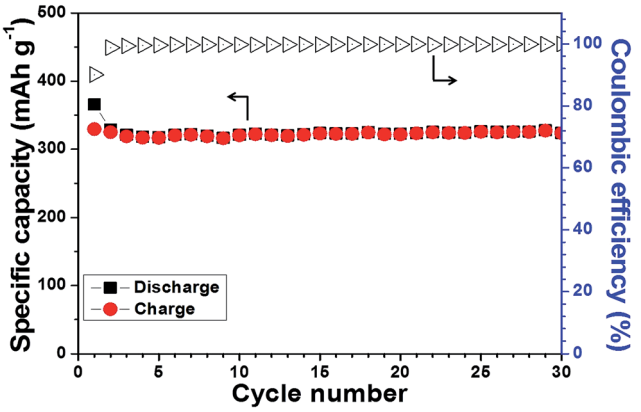

Fig. 9 The cycling stability of graphite anode using PVA–PEI polymer binder.

4. Conclusions

In this study, a low-cost water-soluble PVA–PEI polymer binder has been successfully applied as a high-performance binder for a Si anodes in LIBs. Due to the advantages of a reversibly-deformable polymer network and strong binding between Si and the binder, this binder could effectively accommodate the large volume change of silicon electrodes during the lithiation/delithiation process, resulting in excellent cycling stability (1063.1 mA h g^{-1} after 300 cycles) and high coulombic efficiency (initially 83.8% and rising to 99.3% by the third cycle) at a current density of 1 A g^{-1}. Furthermore, the Si anode with PVA–PEI binder also exhibited a good rate performance and achieved a high specific capacity of 1590 mA h g^{-1} even at high current density of 10 A g^{-1}. This enhanced electrochemical performance was mainly attributed to the interpenetrated network of this binder. In addition, it also can assist in the formation of a stable SEI film on the Si anode, which has been demonstrated by AFM and SEM. Taking the facile preparation and the low-cost and excellent performance of the Si anode into account, this novel water soluble binder has a great potential to be utilized for high-capacity Si anodes in high-energy LIBs.

Acknowledgements

This work was financially supported by Scientific Research Foundation for Startup Researcher, Natural Science Foundations of Ningbo (2015A610257, 2014A610038), the 151 Talents Project of Zhejiang Province. This work was also sponsored by K. C. Wong Magna Fund in Ningbo University. The part of work carried out in SINANO was supported by the National Natural

Science Foundation of China (Grant No. 21473242, 21273273) and the Strategic Priority Research Program of the Chinese Academy of Sciences (Grant No. XDA09010600).

References

1 T. Yim, S. J. Choi, Y. N. Jo, T. H. Kim, K. J. Kim, G. Jeong and Y. J. Kim, *Electrochim. Acta*, 2014, **136**, 112–120.
2 S. Lim, H. Chu, K. Lee, T. Yim, Y. J. Kim, J. Mun and T. H. Kim, *ACS Appl. Mater. Interfaces*, 2015, **7**, 23545–23553.
3 Y. Yao, M. T. McDowell, I. Ryu, H. Wu, N. Liu, L. B. Hu, W. D. Nix and Y. Cui, *Nano Lett.*, 2011, **11**, 2949–2954.
4 K. S. Eoma, T. Joshi, A. Bordes, I. Do and T. F. Fuller, *J. Power Sources*, 2014, **249**, 118–124.
5 X. S. Zhou, A. M. Cao, L. J. Wan and Y. G. Guo, *Nano Res.*, 2012, **12**, 845–853.
6 F. R. Beck, R. Epur, D. Hong, A. Manivannan and P. N. Kumta, *Electrochim. Acta*, 2014, **127**, 299–306.
7 D. He, F. Bai, L. Li, L. Shen, H. H. Kung and N. Z. Bao, *Electrochim. Acta*, 2015, **169**, 409–415.
8 J. Z. Wang, C. Zhong, S. L. Chou and H. K. Liu, *Electrochem. Commun.*, 2010, **12**, 1467–1470.
9 X. W. Zhong, Z. Z. Yang, X. W. Liu, J. Q. Wang, L. Gu and Y. Yu, *ACS Appl. Mater. Interfaces*, 2015, **7**, 18320–18326.
10 A. R. Park, J. S. Kim, K. S. Kim, K. Zhang, J. Park, J. H. Park, J. K. Lee and P. J. Yoo, *ACS Appl. Mater. Interfaces*, 2014, **6**, 1702–1708.
11 T. Song, H. Cheng, Y. K. Town, H. Park, R. W. Black, S. Lee, W. I. Park, Y. J. Huang, A. Rogers, L. Nazar and F. U. Paik, *Adv. Funct. Mater.*, 2014, **24**, 1458–1464.
12 Q. B. Yun, X. Y. Qin, W. Lv, Y. B. He, B. H. Li, F. Y. Kang and Q. H. Yang, *Carbon*, 2015, **93**, 59–67.
13 M. Ko, S. Chae, S. Jeong, P. Oh and J. Cho, *ACS Nano*, 2014, **8**, 8591–8599.
14 Y. Zhu, W. Liu, X. Zhang, J. He, J. Chen, Y. Wang and T. Cao, *Langmuir*, 2013, **29**, 744–749.
15 N. Lia, S. X. Jin, Q. Y. Liao, H. Cui and C. X. Wang, *Nano Energy*, 2014, **5**, 105–115.
16 C. L. Ma, C. Ma, J. Z. Wang, H. Q. Wang, J. L. Shi, Y. Song, Q. G. Guo and L. Liu, *Carbon*, 2014, **72**, 38–46.
17 N. Lin, J. B. Zhou, L. B. Wang, Y. C. Zhu and Y. T. Qian, *ACS Appl. Mater. Interfaces*, 2015, **7**, 409–414.
18 T. Jaumann, M. Herklotz, M. Klose, K. Pinkert, S. Oswald, J. Eckert and L. Giebeler, *Chem. Mater.*, 2015, **27**, 37–43.
19 B. Koo, H. Kim, Y. Cho, K. T. Lee, N. S. Choi and J. Cho, *Angew. Chem., Int. Ed.*, 2012, **51**, 8762–8767.
20 K. W. Kim, H. Park, J. G. Lee, J. Kim, Y. U. Kim, J. H. Ryu, J. J. Kim and S. M. Oh, *Electrochim. Acta*, 2013, **103**, 226–230.
21 Z. Lu, J. Zhu, D. Sim, W. Y. Shi, Y. Tay, J. Ma, H. H. Hng and Q. Yan, *Electrochim. Acta*, 2012, **74**, 176–181.
22 J. M. Yuk, H. K. Seo, J. W. Choi and J. Y. Lee, *ACS Nano*, 2014, **8**, 7478–7485.
23 Y. Du, G. Zhu, K. Wang, Y. Wang, C. Wang and Y. Xia, *Electrochem. Commun.*, 2013, **36**, 107–110.
24 M. Ling, Y. N. Xu, H. Zhao, X. X. Gu, J. X. Qiu, S. Li, M. Y. Wu, X. Y. Song, C. Yan, G. Liu and S. Q. Zhang, *Nano Energy*, 2015, **12**, 178–185.
25 L. W. Zhao, S. H. Han, S. Okada, B. K. Na, K. Takeno and J. Yamaki, *J. Power Sources*, 2012, **203**, 78–83.
26 G. Zhao, L. Zhang, Y. Meng, N. Zhang and K. Sun, *J. Power Sources*, 2013, **240**, 212–218.
27 S. Chen, P. Bao, X. Huang, B. Sun and G. Wang, *Nano Res.*, 2014, **7**, 85–94.
28 X. Zhao, M. Li, K. H. Chang and Y. M. Lin, *Nano Res.*, 2014, **7**, 1429–1438.
29 J. Song, S. Chen, M. Zhou, T. Xu, D. Lv, M. L. Gordin, T. Long, M. Melnyk and D. Wang, *J. Mater. Chem. A*, 2014, **2**, 1257–1262.
30 F. Somodi, C. S. Kong, J. C. Santos and D. E. Morse, *New J. Chem.*, 2015, **39**, 621–630.
31 J. G. Ren, Q. H. Wu, G. Hong, W. J. Zhang, H. Wu, K. Amine, J. Yang and S. T. Lee, *Energy Technol.*, 2013, **1**, 77–84.
32 J. X. Song, M. J. Zhou, R. Yi, T. Xu, M. L. Gordin, D. H. Tang, Z. X. Yu, M. Regula and D. H. Wang, *Adv. Funct. Mater.*, 2014, **24**, 5904–5910.
33 C. Wang, H. Wu, Z. Chen, M. T. McDowell, Y. Cui and Z. Bao, *Nat. Chem.*, 2013, **5**, 1042–1048.
34 I. Kovalenko, B. Zdyrko, A. Magasinski, B. Hertzberg, Z. Milicev, R. Burtovyy, I. Luzinov and G. Yushin, *Science*, 2011, **334**, 75–79.
35 S. Komaba, N. Yabuuchi, T. Ozeki, Z. J. Han, K. Shimomura, H. Yui, Y. Katayama and T. Miura, *J. Phys. Chem. C*, 2012, **116**, 1380–1389.
36 G. Liu, S. Xun, N. Vukmirovic, X. Song, P. O. Velasco, H. Zheng, V. S. Battaglia, L. Wang and W. Yang, *Adv. Mater.*, 2011, **23**, 4679–4683.
37 B. Koo, H. Kim, Y. Cho, K. T. Lee, N. S. Choi and J. Cho, *Angew. Chem., Int. Ed.*, 2012, **51**, 8762–8767.
38 M. H. Ryou, J. Kim, I. Lee and J. W. Choi, *Adv. Mater.*, 2013, **25**, 1571–1576.
39 N. Sahiner, *Colloids Surf., A*, 2013, **433**, 212–218.
40 G. P. Susana, C. A. Luca, H. G. Jose, C. A. George, C. Roberto, A. Athanassia and S. B. Ilker, *Chem. Eng. J.*, 2015, **277**, 242–251.
41 D. C. Lin, Z. D. Lu, P. C. Hsu, H. R. Lee, N. Liu, J. Zhao, H. T. Wang, C. Liu and Y. Cui, *Energy Environ. Sci.*, 2015, **8**, 2371–2376.
42 Z. D. Lu, N. Liu, H. W. Lee, J. Zhao, W. Y. Li, Y. Z. Li and Y. Cui, *ACS Nano*, 2015, **9**, 2540–2547.
43 M. H. Park, M. G. Kim, J. Joo, K. Kim, J. Kim, S. Ahn, Y. Cui and J. Cho, *Nano Lett.*, 2009, **9**, 3844–3847.
44 F. Luo, G. Chu, X. X. Xia, B. N. Liu, J. Y. Zheng, J. J. Li, H. Li, C. Z. Gu and L. Q. Chen, *Nanoscale*, 2015, **7**, 7651–7658.
45 J. Y. Zheng, H. Zheng, R. Wang, L. B. Ben, W. Lu, L. W. Chen, L. Q. Chen and H. Li, *Phys. Chem. Chem. Phys.*, 2014, **16**, 13229–13238.
46 Y. He, X. Yu, G. Li, R. Wang, H. Li, Y. Wang, H. Gao and X. Huang, *J. Power Sources*, 2012, **216**, 131–138.
47 M. T. McDowell, S. W. Lee, J. T. Harris, B. A. Korgel, C. M. Wang, W. D. Nix and Y. Cui, *Nano Lett.*, 2013, **13**, 758–764.
48 J. W. Wang, Y. He, F. F. Fan, X. H. Liu, S. M. Xia, Y. Liu, C. T. Harris, H. Li, J. Y. Huang, S. X. Mao and T. Zhu, *Nano Lett.*, 2013, **13**, 709–715.

